

Calculated electron dynamics in an electric field

F. Robicheaux and J. Shaw

Department of Physics, Auburn University, Auburn, Alabama 36849

(Received 18 December 1996; revised manuscript received 14 February 1997)

We present the details of a theoretical method for calculating the wave-packet dynamics of a Rydberg electron in a strong electric field. Results for Rb are presented, and are compared to recent experiments that measure the time dependence of the electron flux. These interesting experiments provide a different possibility for the experimental detection of wave packets. The results of fully quantum and classical calculations are compared to each other. Several aspects of this system that are easier to study theoretically are presented. The main property that can only be obtained theoretically is the form of the wave function near the nucleus. We found that the flux of electrons entering the detector accurately reflects the flux of electrons leaving a sphere of radius 2000 a.u. centered on the atomic nucleus. The classification of the autoionizing states contributing to the wave packet is also easier to obtain theoretically. [S1050-2947(97)06307-5]

PACS number(s): 32.60.+i, 42.65.Re, 32.80.Dz

I. INTRODUCTION

Recent advances allow the exploration of electron dynamics in atoms in a dynamical fashion [1–20] through the creation and detection of time-dependent electron waves. These waves are often called wave packets, although they may not be very localized in phase space. A pulsed laser field or a pulsed electric field creates the wave packet and determines its initial conditions. The electron wave rapidly evolves in the Coulomb and external fields. Measuring the electron dynamics poses a difficult technological problem that has been solved several different ways. The focus of this paper is on the creation of wave packets in the autoionizing regime for an alkali-metal atom in a strong and static electric field. This is one of the few systems involving more than one degree of freedom that has been explored [21–30].

The time-dependent flux of electrons ejected from autoionizing states of Rb atoms has been measured in a static electric field using an electron streak camera [13]. These striking measurements form a point of comparison between calculations and experiment. The experiments excite Rb from the ground state to autoionizing states just above the classical ionization threshold in the field. These experiments provide a very interesting way to probe the wave packet near the atom. Autoionizing states naturally eject electrons, and these electrons can be detected far from the atom. Wave packets constructed from autoionizing states eject electrons in a periodic fashion that reflects the periodicity of the transiently bound electron.

The wave-packet dynamics is determined by several parameters: the static electric field, the laser polarization, the main frequency of the laser, and the pulse duration. The flux of electrons from the Rb can be a very complicated function of time but the time dependence of this flux reflects the time dependence of the wave packet in the autoionizing states. By varying the parameters, a good match between the calculated and experimental fluxes may be obtained. However, the asymptotic flux is only a small part of the information that may be obtained from the *calculated* wave packet. The calculated wave packet allows the precise determination of the dynamics that led to the measured flux. By linking our com-

putational and experimental efforts, we gain a deeper insight into this dynamical system.

The creation and detection of wave packets allows a somewhat more direct connection to and exhibition of “classical dynamics” in quantum-mechanical systems. Many of the experiments on simple quantum systems have features that may easily be interpreted using classical ideas. Relatively little work has been done on complex systems, especially systems involving two or more coupled degrees of freedom. Wave packets generated on heavy alkali-metal atoms in a strong static electric field are a prototype for the dynamics of complex wave packets. The electric field plus Coulomb potential leads to a separable Hamiltonian in parabolic coordinates; thus the motion is independent in each of the parabolic degrees of freedom. However, for the heavy alkali-metal atoms, the core electrons break the “parabolic symmetry” for the valence electron, causing strong scattering between the different types of parabolic motion. The quantum-mechanical wave function can be described as a superposition of functions in the different parabolic channels, with the core causing a coupling between the channels.

The motion of electron wave packets on alkali-metal ions in constant electric fields provides an ideal setting for comparison between theory and experiment. Further, the dynamics of this system may be calculated in two different ways, with only a modest investment of computational resources. The two methods that are utilized complement each other, in that there are some parameters that may be calculated using either method (e.g., total photoionization cross section) and there are some parameters that can only be obtained using one of the methods. By comparing the results from the two methods where possible, we can gain confidence that we have implemented them both in an accurate and bug-free manner.

The simpler of the two methods to implement constructs the wave packet using a superposition of functions that are solutions of an inhomogeneous Schrödinger equation. These functions depend on the energy, and are constructed by calculating the Green’s function using a basis set of functions in spherical coordinates. The more difficult method to implement constructs wave packets by superposing homogeneous

functions calculated within the formalism developed by Harmin [31] using the local frame transformation suggested by Fano [32]. In this method, the parabolic symmetry of the Hamiltonian outside of the core region is exploited in the construction of the energy-dependent wave function. The core couples together the different parabolic channels, which causes the scattering of the electron from one channel to another.

We have completed some preliminary calculations of the classical dynamics for this system, as well as the exact wave-packet calculations. The connection between *some aspects* of the classical and quantum dynamics should be more easily made using wave packets. In general, we have found this to be true. For the systems that we present in this paper, the connection is sometimes difficult to make, because the wave packets are constructed from relatively few states. Certainly, the connection of our packets to periodic orbits cannot be made cleanly.

The final part of this paper involves the presentation of calculations of electron wave packets for Rb in an electric field. These calculations focus on explaining the experimental results of Lankhuijzen and Noordam [13]. To this end we calculate the frequency-dependent cross section, we calculate the asymptotic flux for one of the experimental geometries, we show several of the wave packets, and we show some of the classical trajectories that seem to have some correspondence with the wave packet. Calculations for another of the experimental geometries has already been presented [33]. Atomic units are used throughout this paper unless specifically noted.

II. LASER PULSE EXCITATION OF WAVE PACKETS

In this paper, we are concerned with the dynamics of wave packets that have been created by shining a weak pulsed laser on an initial state. The wave packet is the solution of the inhomogeneous Schrödinger equation

$$\left(i \frac{\partial}{\partial t} - H\right) \psi(\vec{r}, t) = F(t) \hat{\epsilon} \cdot \vec{r} \cos \omega_0 t \exp(-iE_I t) \psi_I(\vec{r}), \quad (1)$$

where H is the static Hamiltonian incorporating the atomic Hamiltonian and the potential from the static electric field, $\psi_I(\vec{r})$ is the initial state, E_I is the initial state energy, ω_0 is the main frequency of the laser pulse, $\hat{\epsilon}$ is the polarization, and $F(t)$ is the relatively slowly varying laser envelope. The function $\psi(\vec{r}, t)$ may be obtained in several different ways. Two methods based on time-dependent perturbation theory may be used. Both methods use a Fourier decomposition of the laser envelope

$$\mathcal{F}(\Omega) = \int_{-\infty}^{\infty} F(t) e^{i\Omega t} dt. \quad (2)$$

The quantity $\mathcal{F}(\omega - \omega_0)$ is proportional to the amplitude for finding a photon of frequency ω in the laser pulse. The function $\mathcal{F}(\Omega)$ is strongly peaked around $\Omega = 0$, which gives a strong peaking of the photon amplitude near $\omega = \omega_0$.

We are interested in calculating wave packets of continuum states. This makes the construction of wave packets

slightly more difficult than the usual case where the packets are constructed from bound states. It is now necessary to superpose an infinite number of states. The wave packet can be constructed by superimposing the solutions of the inhomogeneous Schrödinger equation

$$(E - H) \Lambda_E^+(\vec{r}) = \hat{\epsilon} \cdot \vec{r} \psi_I(\vec{r}), \quad (3)$$

where the $+$ superscript indicates that Λ_E^+ is composed of outgoing waves in *every* open channel. By simple substitution into Eq. (1), it is possible to show that

$$\psi(\vec{r}, t) = \frac{1}{4\pi} \int \Lambda_E^+(\vec{r}) e^{-iEt} \mathcal{F}(E - E_I - \omega) dE \quad (4)$$

where the rotating-wave approximation has been used (i.e., the $\exp[-i(E_I - \omega)t]$ term in Eq. (1) is neglected).

The wave packet may also be constructed by superimposing the solutions of the homogeneous Schrödinger equation

$$(E - H) \Psi_{E\beta}^-(\vec{r}) = 0. \quad (5)$$

For energies in the continuum, there are, in general, several open channels at energy E . The number of linearly independent solutions, N , equals the number of open channels. There are infinitely many different ways of constructing the linearly independent solutions, so we will choose the linearly independent solutions in a form that will most easily allow the construction of the outgoing flux. These functions, $\Psi_{E\beta}^-$, are constructed so that asymptotically they *only* have outgoing waves in channel β . These functions have the general orthogonality property

$$\langle \Psi_{E\beta}^- | \Psi_{E'\beta'}^- \rangle = O_{\beta\beta'} \delta(E - E'), \quad (6)$$

where often the overlap matrix $O_{\beta\beta'} = \delta_{\beta\beta'}$ (the overlap matrix is not proportional to δ functions for the outgoing waves in parabolic coordinates, which forces us to use the more general formalism). In terms of these functions, the wave packet may be constructed for times after the laser pulse has gone to zero as

$$\psi(\vec{r}, t) = -\frac{i}{2} \sum_{\beta} \int D_{E\beta}^- \Psi_{E\beta}^- e^{-iEt} \mathcal{F}(E - E_I - \omega) dE, \quad (7)$$

where the dipole matrix elements for these functions have the general form

$$D_{E\beta}^- = \sum_{\beta'} (O^{-1})_{\beta\beta'} \langle \Psi_{E\beta'}^- | \hat{\epsilon} \cdot \vec{r} | \psi_I \rangle. \quad (8)$$

The two methods presented above give equivalent results. But there are advantages to using different methods in different regions of space, as will be described below. An important point of contact between the different methods is the total photoionization cross section. The total cross section may be obtained as

$$\sigma(E) \propto \omega \sum_{\beta} |D_{E\beta}^-|^2 \propto \omega \text{Im}[\langle \psi_I | \hat{\epsilon} \cdot \vec{r} | \Lambda_E^+ \rangle]. \quad (9)$$

This relationship may be exploited as a test of the implementation of the different methods.

It is important to note that nothing in this section depends on the particular problem that is being examined. The only requirement is that H be time independent, and that the excitation be perturbative. We note that several dynamical situations may be examined immediately using existing computer programs and Eqs. (4) and (7). In particular, wave packets excited in constant electric *and* magnetic fields or only in magnetic fields may be explored. These problems may have deep interest, since it would be possible to excite wave packets for parameter ranges that would lead to chaos in classical mechanics.

III. CALCULATING Λ_E^+

One method for calculating the wave packet is to superimpose the inhomogeneous functions that are solutions of Eq. (3). The $\Lambda_E^+(\vec{r})$ are the solutions with outgoing waves in *every* open channel. Enforcing this large distance boundary condition in an elegant and accurate manner is very difficult. However, a brute force approach borrowed from codes involving the direct solution of the time-dependent Schrödinger equation will give an accurate Λ^+ without the need for an explicit solution of the boundary conditions.

The inhomogeneous equation was solved by expressing $\Lambda_E^+(\vec{r})$ as a superposition of radial functions times spherical harmonics. The radial functions were the solution of the radial Rb Hamiltonian with a model potential near the origin to give the correct quantum defects for the atom. The radial functions were orthonormal since they were all generated from the same potential, and they were all forced to zero at $r=2800$ a.u. We used 89 radial functions for each ℓ , and a maximum ℓ of 59. Convergence was tested by increasing the number of radial functions by ten, keeping everything else fixed, or by increasing the maximum ℓ by ten and keeping everything else fixed. Neither increase changed the results by more than 0.5%.

The inhomogeneous function was calculated by direct solution for x in the $\mathbf{Ax}=\vec{b}$ linear problem, taking full advantage of the block-tridiagonal nature of H . The algorithm was based on the formal solution of a tridiagonal linear equation, except that the elements of the tridiagonal linear system were themselves matrices. This allowed the calculation of Λ_E^+ to be roughly 100–1000 times faster than when working with the full Hamiltonian matrix of the same size. This speed was crucial, because Λ_E^+ needed to be calculated at several hundred energy points for each set of experimental parameters.

The description to this point leaves out the important description of how to obtain the correct asymptotic boundary conditions. Remember, $\Lambda_E^+(\vec{r})$ *must* have outgoing waves in *all* of the open channels with incoming waves in *none* of the open channels. The correct boundary conditions are automatically incorporated if we add to H an unphysical imaginary potential. The imaginary potential decreases the norm of the wave function, where the imaginary potential is non-zero. The requirement on the absorbing potential is that it absorbs the vast majority of the flux moving to large r and does not absorb flux at an r that is too small, thus affecting the autoionizing dynamics. Two possible problems with the

TABLE I. Parameters for the Rb model potential.

ℓ	$\alpha_\ell^{(1)}$	$\alpha_\ell^{(2)}$	$\alpha_\ell^{(3)}$
0	4.1240	9.0613	1.7143
1	4.2865	9.6776	1.7418
2	4.0049	9.1774	1.8157
3+	4.0049	9.1774	1.8207

absorbing potential must be avoided. First, the absorbing potential should not turn on so quickly in r that it reflects electrons back into the region of small r . Second, the absorbing potential should not be so weak that the electron can travel all of the way to $r=2800$ a.u. and reflect back into the small- r region. Both these restrictions can be satisfied for our wave packets, because we are working in a very narrow energy range.

The only drawback to using this method for constructing wave packets is that it cannot be used to compare with the experimental results of Lankhuijzen and Noordam [13] without first comparing to some other computational technique. In these experiments, the time dependent flux of electrons ejected from alkali atoms in static E fields was measured in a time-dependent manner using an electron streak camera. Unfortunately, the electrons ejected from Rb may not exactly maintain their spatial relationship as they travel from the atom to the detector. This dispersion may prevent a quantitative comparison to their experiments using the superimposition of $\Lambda_E^+(\vec{r})$ that are constructed from a finite basis. A comparison of the flux obtained from this method with a computational technique that calculates the flux a macroscopic distance from the atom would also allow us to answer the question: How faithfully does the time-dependent flux entering the detector reflect the dynamics near the atom?

An interesting aspect of this method involves its flexibility. Any type of alkali-metal atom in a static field can be described with this method. There does not appear to be any reason why we could not make wave packets on any of the heavily explored field atom combinations: magnetic fields and parallel E and B fields, for example.

The zero-field Rb radial functions were generated using a model potential of the form

$$V_\ell(r) = -\frac{Z_\ell(r)}{r} - \frac{\alpha_d}{2r^4} \{1 - \exp[-(r/r_c)^3]\}^2 + \frac{\ell(\ell+1)}{2r^2}, \quad (10)$$

where $\alpha_d=9.076$ is the dipole polarizability of Rb^+ [34], $r_c=1.0$, and $Z_\ell(r) = 1 + 36\exp(-\alpha_\ell^{(1)}r) + \alpha_\ell^{(2)}r\exp(-\alpha_\ell^{(3)}r)$, with the α_ℓ given in Table I. This potential gives quantum defects with errors less than 0.002 for $\ell \leq 3$. The radial functions were generated on a grid of radial points on a square root mesh in r (i.e., equally spaced points in s where $r=s^2$). The derivatives in the one electron Hamiltonian were approximated by a five-point or fourth-order finite difference. The orbitals were generated using a relaxation technique by repeated multiplication of a trial $R_{n\ell}$ by $[E_{n\ell} - H_\ell]^{-1}$. Usually, only two or three multiplies were needed to achieve convergence to double precision roundoff accuracy.

IV. CALCULATING HOMOGENEOUS PARAMETERS

The dynamical system of an alkali-metal atom in a static electric field was theoretically described by Harmin [31] based on a method suggested by Fano [32]. This method is ideally suited to describe the detection of electron flux far from the atom, since the dipole matrix elements of Eq. (7) and the asymptotic form of the Ψ^- functions are generated. The cross section may be obtained from the dipole matrix elements, forming a point of contact with the method of Sec. III. We recast the derivation of Ref. [31] into a form more amenable to a calculation of the asymptotic time-dependent flux.

The basic idea of this method is that the wave function near the core is well described by standard radial Coulomb function (shifted in phase by π times the quantum defect) times the appropriate spherical harmonic. Outside of the core region the electron moves in a pure Coulomb potential plus static electric field. This type of Hamiltonian can be separated into parabolic coordinates. The solutions in spherical coordinates are connected to the solutions in parabolic coordinates at a distance larger than the core radius, but at a distance small enough that the electric field has not distorted the electron motion; this requirement can always be satisfied for the small experimental electric fields.

The parabolic coordinates are connected to spherical coordinates through

$$\xi = r + z, \quad \eta = r - z, \quad \phi = \arctan(y/x), \quad (11)$$

where $0 \leq \xi$ and $0 \leq \eta$. In terms of these coordinates, the wave function may be written as a superimposition of separable functions

$$\begin{aligned} \psi_{E\beta m}(\xi, \eta, \phi) &= \frac{1}{\sqrt{2\pi\xi\eta}} \Xi_{E\beta m}(\xi) f_{E\beta m}(\eta) e^{im\phi}, \\ \chi_{E\beta m}(\xi, \eta, \phi) &= \frac{1}{\sqrt{2\pi\xi\eta}} \Xi_{E\beta m}(\xi) g_{E\beta m}(\eta) e^{im\phi}, \end{aligned} \quad (12)$$

where f and g are the regular and irregular solutions of

$$\frac{d^2 y(\eta)}{d\eta^2} + \left[\frac{E}{2} - 2 \left(\frac{\beta-1}{2\eta} - \frac{F\eta}{8} + \frac{m^2-1}{8\eta^2} \right) \right] y(\eta) = 0, \quad (13)$$

and Ξ are solutions of solution of

$$\frac{d^2 \Xi(\xi)}{d\xi^2} + \left[\frac{E}{2} - 2 \left(-\frac{\beta}{2\xi} + \frac{F\xi}{8} + \frac{m^2-1}{8\xi^2} \right) \right] \Xi(\xi) = 0, \quad (14)$$

with m the azimuthal quantum number and β the separation constant. The differential equations were written in this form in order to draw attention to generic properties of these functions. The terms in the square brackets play the role of a squared wave number (or equivalently a squared momentum), and the terms in parentheses play the role of a potential. As ξ goes to infinity the potential goes to positive infinity, which means there is only bounded motion in this direction. There is an infinite number of bound states, and as the number of nodes in this direction increases (for a fixed

E), β monotonically increases. As η goes to infinity the potential goes to minus infinity, which means that at every energy there is a continuum wave solution. However, for energies $E < -2\sqrt{(1-\beta)F}$, the electron must tunnel through a potential barrier to go from regions near the core to large distances.

Since the direction for escape is in the η direction, we will think of motion in this direction as longitudinal motion, and motion in the ξ direction as transverse motion. As the amount of energy in transverse motion increases (i.e., as n_ξ increases) there is less energy available to surmount the barrier and escape. At a fixed energy $-2\sqrt{(1-\beta)F}$ will become larger as n_ξ increases, and eventually the electron will be forced to tunnel to escape. When $\beta > 1$, the potential in Eq. (14) is purely repulsive, and an electron would need to tunnel enormous distances to reach the core region. Channels with $\beta > 1$ play no role in the dynamics discussed in this paper.

Following Ref. [31], the functions in Eqs. (13) and (14) are evaluated using WKB-type approximations. This is necessary because of the large number of energies that are needed in the construction of the wave packet. As a technical detail, all of the integrals were calculated numerically using Chebyshev quadrature with less than 40 quadrature points.

For the sake of numerical stability we normalized the $f_{E\beta m}(\eta)$ and $g_{E\beta m}(\eta)$ functions, so that for small η they oscillate 90° out of phase and are energy normalized. The key point of analysis is the connection between the $\psi_{E\beta m}$ and $\chi_{E\beta m}$ functions of Eq. (12) to the functions in spherical coordinates near the core $\psi_{E/m} = f_{E/m}(r) Y_{l,m}$ and $\chi_{E/m} = g_{E/m}(r) Y_{l,m}$ (where $f_{E/m}$ and $g_{E/m}$ are the energy normalized radial Coulomb functions of Ref. [35]) and the connection of the small- η behavior to the functions at asymptotically large η . Note that in this section the symbols Ψ , ψ , and χ mean different things depending on their subscripts; E/m subscripts mean simple functions in spherical coordinates, and $E\beta m$ subscripts mean simple functions in parabolic coordinates.

An atom that has quantum defects $\mu_{/}$ has wave functions near the nucleus $\Psi_{E/m} = \psi_{E/m} - \chi_{E/m} \tan(\pi\mu_{/})$, when r is greater than the size of the core, r_c . The connection between the functions in spherical coordinates to those in parabolic coordinates is accomplished through the local frame transformations [31,32]

$$\psi_{E/m} = \sum_{\beta} (1/U^0)_{/ \beta} \psi_{E\beta m}, \quad (15)$$

$$\chi_{E/m} = \sum_{\beta} \chi_{E\beta m} U_{\beta /}^0, \quad (16)$$

where U^0 is the transformation matrix [Eqs. (17), (21), and (62) of Ref. [31(b)]]. The transformation matrix is real and depends on $E, /, \beta, m$, and $d\beta/dn_1$, although we have only indicated the β and $/$ dependence. The U^0 matrix has a slow energy dependence compared to the U matrix that was used to calculate the cross section in Ref. [31]. We define a standing wave, coupled-channel solution of the Schrödinger equation near the core to be

$$\Psi_{E\beta m} \equiv \sum_{\beta'} U_{\beta'}^0 \Psi_{E/m} = \psi_{E\beta m} - \sum_{\beta'} \chi_{E\beta' m} K_{\beta' \beta}, \quad (17)$$

where the K is the parabolic K matrix that couples the parabolic channels. The coupling arises from the phase shifts due to the core

$$K_{\beta' \beta} = \sum_{\beta''} U_{\beta''}^0 U_{\beta'}^0 \tan(\pi \mu_{\beta''}). \quad (18)$$

Therefore, it is *only* the $\mu_{\beta} \neq 0$ that cause the scattering between parabolic channels.

The connection between the small- η and large- η forms of the $\Psi_{E\beta m}$ function is accomplished through a WKB-type approximation. The functions in η have the asymptotic form given by Eqs. (44) in Ref. [31(b)]. The asymptotic form is needed in order to obtain the flux into the detector.

To this point, we have exactly followed Ref. [31] for describing alkali-metal atoms in static fields. Now we need to slightly modify this approach in order to cast all parameters in a form that will simplify the description of wave packets at asymptotically large distances from the atom. To this end we define new sets of parameters. If we use the definitions

$$\begin{aligned} \bar{R}_{\beta} &= R_{\beta} \exp\left[i\left(\frac{\pi}{4} + \delta_{\beta}\right)\right], \\ \bar{S}_{\beta} &= S_{\beta} \exp\left[i\left(\frac{\pi}{4} + \delta_{\beta} - \gamma_{\beta}\right)\right], \end{aligned} \quad (19)$$

the wave function that only has outgoing waves in each channel β is obtained by

$$\begin{aligned} \Psi_{E\beta m}^{-} &= \sum_{\beta'} \Psi_{E\beta' m} [(\bar{R} - \bar{S}K)^{-1}]_{\beta' \beta} \\ &= \frac{1}{2i} \sum_{\beta'} (\psi_{E\beta' m}^{+} \delta_{\beta' \beta} - \psi_{E\beta' m}^{-} S_{\beta' \beta}^{\dagger}) \end{aligned} \quad (20)$$

where \bar{R} and \bar{S} are diagonal matrices with the elements given by Eq. (19). The δ_{β} [Eq. (49) of Ref. [31(a)]], γ_{β} [Eq. (A9) of Ref. [31(b)]], R_{β} and S_{β} [Appendix A of Ref. [31(b)]] have convenient definitions in terms of WKB integrals. R_{β} and S_{β} are large when the electron must tunnel through the barrier *except* when the WKB integral $\int k(\eta) d\eta$ between the smallest two turning points equals an integer times π for S_{β} or an integer plus $\frac{1}{2}$ times π for R_{β} . The matrix S is the nonunitary S matrix coupling the parabolic channels that is defined by the matrix equation

$$S^{\dagger} = (\bar{R}^* - \bar{S}^* K)(\bar{R} - \bar{S} K)^{-1}, \quad (21)$$

and the asymptotic traveling wave solutions are given by

$$\psi_{E\beta m}^{\pm} \rightarrow \frac{\exp(im\phi)}{\pi \sqrt{\xi \eta k(\eta)}} \Xi_{E\beta m}(\xi) \exp\left[\pm i \int^{\eta} k(\eta') d\eta'\right]. \quad (22)$$

Using Eqs. (17) and (20), we can find an expression for the dipole matrix element in terms of parameters that can be obtained using WKB expressions

$$\langle \Psi_{E\beta m}^{-} | \hat{\epsilon} \cdot \vec{r} | \Psi_I \rangle = \sum_{\beta' \neq \beta} [(\bar{R}^* - K \bar{S}^*)^{-1}]_{\beta \beta'} U_{\beta'}^0 D_{\beta' m}, \quad (23)$$

where $D_{\beta' m} = \langle \Psi_{E/m} | \hat{\epsilon} \cdot \vec{r} | \Psi_I \rangle$ is the dipole matrix element coupling initial and final states when there is zero field. For the systems studied in this paper, the initial state is an s state, so we may take $D_{\beta' m} = \delta_{\beta' 1}$, with the only inaccuracy being the overall size of the cross section or the amount of wave function excited. None of the time or energy dependences are affected by this choice.

The overlap matrix in Eq. (6) may be obtained from the form of Ψ^{-} in Eq. (20) to be

$$O_{\beta \beta'} = \frac{1}{2} \left(\delta_{\beta \beta'} + \sum_{\beta''} S_{\beta \beta''}^{\dagger} S_{\beta'' \beta'} \right). \quad (24)$$

Simple substitution of Eq. (21) into Eq. (24) gives a form for the inverse of this matrix that is numerically unstable when there are several strongly closed channels because R_{β} and S_{β} are very large which gives a nearly singular matrix. If we perform several matrix manipulations and use the identity $R_{\beta} S_{\beta} \sin \gamma_{\beta} = 1$, we obtain the stable form

$$\begin{aligned} (O^{-1} D^{-})_{\beta} &= i \exp\left[i\left(\delta_{\beta} + \frac{\pi}{4}\right)\right] \sum_{\beta' \beta''} (1 + i R^{-1} K W^T)_{\beta \beta'} \\ &\quad \times \{[(1 + W K R^{-2} K W^T)^{-1}] W\}_{\beta' \beta''} U_{\beta''}^0, \end{aligned} \quad (25)$$

where $W = R^{-1}(1 - K R^{-2} \cot \gamma)^{-1}$, and W^T is the transpose of W .

V. CLOSED-ORBIT THEORY AND CLASSICAL TRAJECTORY CALCULATIONS

A. Classical recurrences

The wave-packet description in the previous sections can be related to the classical dynamics of the electron by constructing the semiclassical approximation to the overlap integral in Eq. (9). Let us review this briefly. If a laser excites outgoing waves Λ_E^{+} near the zero field threshold, then those waves go out far from the alkali core, 100–1000-bohr radii. Those portions of the outgoing wave that are turned around in the combined Coulomb and electric field to return to the atomic core follow the paths of the closed classical orbits of the system. These waves return to the source and overlap with it, contributing to the matrix element $\langle \hat{\epsilon} \cdot \vec{r} \psi_I | \Lambda_E^{+} \rangle$ in Eq. (9). The matrix element in Eq. (9) becomes a coherent sum of overlap integrals due to waves associated with distinct classical orbits labeled by (n, k) , i.e., the n th return of the k th orbit. Each orbit gives a sinusoidal modulation in the oscillator strength with an energy wavelength $\lambda_k^n = h/T_k^n$, where T_k^n is the return time of the closed orbit. Closed-orbit theory give formulas for the amplitudes and phases of these modulations [36–38]. The sum of these modulations add up, in principle, to the peaks seen in the photoabsorption spectrum. It is worth emphasizing here that the closed orbits for an alkali-metal atom and hydrogen are the same, since the dynamics outside the core is controlled by the external field

and a $1/r$ attractive potential. The only differences are in the handling of the outgoing and returning waves near the core [37].

To determine the amplitude of the modulations in the spectrum from an orbit, you need to know the shape of the outgoing wave $\mathcal{Y}(\theta_i)$ created by the laser [Eq. (5.12) in Ref. [37]]. This is simple if the initial state is an s state since the dipole operator of the laser can only populate p states. The laser polarization selects whether an outgoing $m=0$ p wave or an outgoing $|m|=1$ p wave is excited. For the rubidium calculations in Sec. VI, the outgoing wave at $t=0$ is $\ell=1$, $|m|=1$, so a closed orbit going out at an initial angle $\theta_i^{k,n}$ is weighted by $\sin(\theta_i^{k,n})$. Orbits going out near the electric-field axis $\theta_i=0$ are suppressed, while those going out near $\theta_i=90^\circ$ are emphasized.

This gives the initial amplitude of the outgoing wave near the initial angle of the outgoing classical closed orbit. Starting on an initial surface $10 \leq r_o \leq 100$ bohr, we use a semiclassical approximation to the Green's function, $G^{\text{sc}}(\vec{r}, \vec{r}_o) = A(\vec{r}, \vec{r}_o) e^{i\Delta(\vec{r}, \vec{r}_o)}$, to propagate the waves along the classical paths connecting $\vec{r}_o = (r_o, \theta_i^{k,n}, 0)$ and $\vec{r} = (r, \theta, \phi)$ [39]. The phase Δ of this wave function depends on the classical action along the path S_k^n , and the Maslov index μ_k^n , which counts the number of caustics and foci encountered on the orbit [39,40]. The semiclassical amplitude $A(\vec{r}, \vec{r}_o)$ depends on the divergence rate of the neighboring trajectories. For closed orbits the amplitude $A(\vec{r}, \vec{r}_o)$ is related to the stability properties of the closed orbit [41].

For closed orbits, we connect the semiclassical returning wave to the partial wave expansion, $\Psi_{\theta_f}^{\text{pw}}(r, \theta)$, for a zero-energy wave coming in from infinity at a particular final angle $\theta_f^{k,n}$ [Eq. (7.5) in Ref. [37]]. The ratio of the semiclassical returning wave to the incoming part of an incoming zero-energy scattering wave defines a complex matching constant N_k^n , which multiplies $\Psi_{\theta_f}^{\text{pw}}(r, \theta)$ for each closed orbit. N_k^n contains the amplitude and phase of the returning wave for the n th return of the k th closed orbit. An expression for this matching constant when $\theta_i^{k,n} \neq 0$ is given as Eq. (7.10) in Ref. [37]. The phase of the returning wave is set by the action and Maslov indices calculated from the origin to the origin on an orbit. The amplitude reduces to terms involving the derivative of $\theta_f^{k,n}$ with respect to θ_i^k evaluated on a boundary r_o and is proportional to $\mathcal{Y}(\theta_i^{k,n})$.

Therefore the returning part of the wave Λ_E^+ in the semiclassical approximation is

$$\Lambda_{E,k}^{\text{ret},n}(\vec{r}) = N_k^n \Psi_{\theta_f}^{\text{pw}}(r, \theta). \quad (26)$$

This lets us define the recurrence integral for the n th return of the k th orbit as

$$R_k^n \equiv \langle \epsilon \cdot \vec{r} \psi_I | \Lambda_{E,k}^{\text{ret},n} \rangle = \frac{4\pi}{\sqrt{2}} \mathcal{Y}(\theta_f^{k,n}) N_k^n \quad (27)$$

since the overlap of $\langle \epsilon \cdot \vec{r} \psi_I |$ with $\Psi_{\theta_f}^{\text{pw}}(r, \theta)$ [see Eq. (7.7) in Ref. [37]], is just $2^{3/2} \pi \mathcal{Y}(\theta_f)$ (the \mathcal{Y} here is the ‘‘unexpected’’ conjugate [37] of \mathcal{Y} evaluated at the final angle of the incoming wave).

R_k^n gives the amplitude and phase of the terms in the oscillator strength due to each closed hydrogenic orbit. We will show in Sec. V B that writing the recurrences in terms of the recurrence integral allows us to simplify the scattering calculations. Figure 5 shows the closed classical orbits relevant to the study of Rb. We will use Eq. (27) in Sec. VI when looking at classical recurrence time versus the time of flux ejection from the region of the core.

B. Semiclassical core scattering

The formulas above *partially* account for the non-Coulombic field within the core. For example the angular functions $\mathcal{Y}(\theta)$ contain the phase shifts $\pi \mu_\ell$ which are related to the quantum defects. However, returning waves on the k th closed orbit create core-scattered outgoing waves on *all* the closed orbits, including the original orbit, and this is not accounted for in Eq. (27). Core scattering in effect constitutes a new source: the core-scattered outgoing waves can be turned around by the external fields, and return to the atom and produce a whole new set of recurrences. In an electric field, the core-scattered outgoing waves can also go out in directions that lead to ionizing trajectories [for example, see Fig. 5(c)] [33]. This is the semiclassical analog to the channel coupling that leads to ionization in the quantum calculations. To obtain the quantitative description of the scattering, it helps to define new notation.

The core-scattered wave can be extracted from the partial-wave expansion $\Psi_{\theta_f}^{\text{pw}}(r, \theta)$, Eqs. (7.14a) and (7.14b) in Ref. [37], so the core-scattered wave created by the n_1 return of the k_1 hydrogenic orbit is $N_{k_1}^{n_1}$ times the core-scattered part of $\Psi_{\theta_f}^{\text{pw}}(r, \theta)$. If we semiclassically propagate that part of the core-scattered wave that goes out in the direction of the k_2 closed orbit, and take the overlap after n_2 cycles on the new closed orbit, then we obtain a ‘‘combination-recurrence’’ integral given by

$$R_{k_2 k_1}^{n_2 n_1} = R_{k_2}^{n_2} \frac{T_{k_2 k_1}^{n_1}}{\mathcal{Y}(\theta_i^{k_2}) \mathcal{Y}(\theta_f^{k_1, n_1})} R_{k_1}^{n_1}, \quad (28)$$

where the \mathcal{Y} 's in the denominator of $R_{k_2 k_1}^{n_2 n_1}$ cancel corresponding factors in the R 's for each orbit. The angular dependence of $T_{k_2 k_1}^{n_1}$ is proportional to the usual T matrix; we use the definition

$$T_{k_2 k_1}^{n_1} = \frac{i}{4\pi} \sum_{\ell \geq |m|} (e^{2i\pi\mu_\ell} - 1) Y_{\ell m}(\theta_i^{k_2}, 0) Y_{\ell m}^*(\theta_f^{k_1, n_1}, 0), \quad (29)$$

where m is the azimuthal quantum number appropriate to the laser polarization. The combination-recurrence integral is proportional to the recurrence integrals for both the first and second orbits, and $T_{k_2 k_1}^{n_1}$ constitutes an effective T matrix representing the scattering by the core from one orbit to another. By splitting the scattering expression into the recurrence integrals for each closed orbit, and a coupling term which depends only on the incoming and outgoing angles, we can simplify the multiple-scattering expansions derived

in Ref. [42], and generalize to include outgoing angles that lead to ionizing trajectories in the electric field.

Equation (29) was derived by taking the outgoing angle of the scattered wave, θ , to be the initial angle $\theta_i^{k_2}$ of a new closed orbit. Dropping this restriction gives an expression for the scattered wave which is proportional to the recurrence integral of the original closed orbit times a scattering amplitude for scattering from a closed orbit (n_1, k_1) into the direction θ_i . As we will see in this experiment with rubidium, if the recurrences described by Eq. (27) are not resolved and interfere destructively, then this predicts that the flux of electrons ejected from the atom will be small. This connects the classical recurrences to the delayed flux ejection.

VI. SPECIFIC CASES IN Rb

In this section, we describe the knowledge gained from the calculated dynamics of a Rb electron wave packet in a field of ~ 2 kV/cm. We have chosen this case because we can compare our calculated time-dependent flux to the measurements of Lankhuijzen and Noordam [13]. We are only examining cases for which the electron can classically escape to the detector, i.e., $E > -2\sqrt{F}$. Before presenting the specific cases, we will first discuss some of the generic properties of a highly excited alkali-metal atom in a strong electric field.

A. Generic properties

The electric field that we will use in this is small compared to the atomic unit of field strength; we will be utilizing $F \sim 4 \times 10^{-7}$ a.u. But the states that we examine will be highly excited, and Fz will not be a perturbative interaction. Certainly, since we will be interested in energies $0 \geq E \geq -2\sqrt{F}$, the electron dynamics will be strongly influenced by the electric field. This is the energy range that a classical electron can escape the atom and travel to the detector if the field is on but not if the field is off. A measure of the nonperturbative nature of this interaction is the size of the zero-field basis used in the calculation of the $\Lambda_E^+(\vec{r})$; ~ 90 radial functions per ℓ and $\sim 60\ell$ channels. This is very large considering we are exciting $n \sim 20$ states which perturbatively can only mix in ℓ up to ~ 20 .

If the atom in the electric field is hydrogen, all of the quantum defects in Eq. (18) are zero, and thus the couplings between the parabolic channels is zero. A wave packet on hydrogen in an E field will consist of several independent waves oscillating in the different parabolic channels. For energies $E < -2\sqrt{F}$, the electron can only escape by tunneling. If $E > -2\sqrt{F}$, there will be several channels (small n_ξ) in which the electron can escape the atom by going over the top of the barrier, and there will be several channels (large n_ξ) in which the electron can only escape the atom by tunneling. Qualitatively, the more energy in the ξ coordinate (this energy increases with the number of nodes, n_ξ) the less energy is available in the η direction to escape over the barrier. As n_ξ increases, the tunneling rate decreases and the lifetime increases. The behavior of a wave packet on H in the range $0 \geq E \geq -2\sqrt{F}$ can be described as follows: (1) The part of the wave packet with n_ξ small enough so the electron does not need to tunnel to escape the atom will have waves start-

ing near the nucleus that travel over the barrier directly to the detector with nearly unit probability. (2) The part of the packet with n_ξ too large will have waves starting near the nucleus that travel to the barrier. Because they do not have enough energy to go over the barrier, most of the wave is reflected back to small η , while a small fraction of the wave tunnels through the barrier and then travels to the detector. The part of the wave reflected from the barrier travels back to small η , where it is completely reflected back to large η in the same parabolic channel. Thus the flux of electrons from the atom will have a peak that comes from electrons that directly escape the atom, and several later pulses that arise from electrons getting close to the barrier and tunneling through. The electron flux gives a measure of finding the electron near enough to the barrier to tunnel through.

If the atom in the electric field is Li, Na, K, Rb, or Cs, some of the quantum defects in Eq. (18) are nonzero, and thus there is a coupling between the parabolic channels. Remember that this arises because the core electrons break the parabolic symmetry for the valence electron. All of the discussion for H in the previous paragraph remains true except for the coupling between the parabolic channels. This small difference *qualitatively* changes the wave packet dynamics by giving a *third* mechanism for ejecting flux from the atom. (3) After scattering from the nucleus, some of the wave packet will be in channels with small enough n_ξ to directly escape over the barrier; this occurs in the alkali-metal atoms because the core breaks the parabolic symmetry scattering some of the electron wave from channel β to channel β' . Thus the flux of electrons from the atom will have a direct peak that comes from electrons that directly escape the atom, and later pulses that arise from electrons getting close to the barrier and tunneling through, *and* later pulses that arise from electrons scattering from the core into channels for which the electron can directly escape the atom. Except for large- m states (large m being defined to be such that $\mu_\ell \ll 1$ for $\ell \geq m$) the main mode of ejection of electrons from later pulses arises from mechanism (3) (i.e., the electron is more likely to scatter from the core into classically open channels than to tunnel through the barrier in the closed channels). For later pulses, the electron flux gives a measure of finding the electron near the core in an angular momentum state small enough to scatter into open channels.

B. Results

A comparison between the experimental and calculated electron fluxes was presented in Ref. [33] for a case of linear polarization. For this case we were able to obtain excellent agreement. Several interesting effects were noted in this paper. We were also able to relate the time-dependent flux to a single orbit because only one of the orbits had a large amplitude for excitation by a laser polarized in the static field direction. The difference between the classical period and the measured period could be explained by trimming the autoionizing states.

In this section, we will present additional results comparing calculated and experimental time-dependent fluxes for a case where the laser is polarized perpendicular to the static field. This case has several interesting features, which we

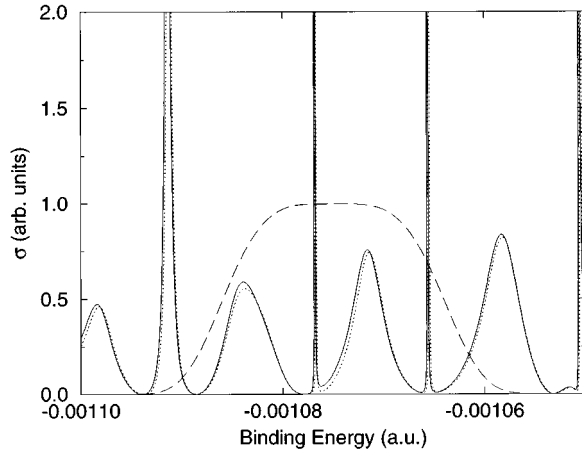


FIG. 1. Solid line, proportional to the infinite resolution photoionization cross section as a function of the electron's energy: $F_{\text{stat}}=2005$ V/cm and $m=1$ from the homogeneous function. Dotted line, same except using the inhomogeneous function. Dashed line, proportional to $\mathcal{F}(E)$, the amplitude for finding a photon at each energy.

will present. The experimental results were previously presented in Fig. 3 of Ref. [13].

All of the results in this paper are for the pulsed-laser excitation of Rb atoms in a static electric field of 3.90×10^{-7} a.u. = 2005 V/cm. The Rb atoms are initially in the $5s$ ground state which is unperturbed by the weak static field. The laser excites two wave packets: one with azimuthal quantum number $m=1$ and one with $m=-1$. These two packets do not interfere with each other, since the detector averages over ϕ and contribute equivalent amounts to the measured flux in the detector. The flux into the detector is simply twice the flux from the $m=1$ packet. Therefore, all calculations are performed only for $m=1$ packets. This has the added advantage that the resulting $|\psi|^2$ has an azimuthal symmetry, making it easier to display. Since the dipole coupling in Eq. (23) is only to $\ell=1$, the specific value of this matrix element only provides an overall size but does not affect the dynamics. The only dynamical information that is necessary is the quantum defects. We have used the values $\mu_0=3.14$, $\mu_1=2.64$, $\mu_2=1.348$, $\mu_3=0.016$, and $\mu_{\ell \geq 4}=0$. From these values it is clear that the main scattering between the parabolic channels occurs for $\ell \leq 2$. The main frequency of the laser pulse is such that the atom is excited to the autoionizing threshold in a 2.005-kV/cm field and the zero-field ionization threshold.

In Fig. 1, we present the infinite resolution photoionization cross section versus binding energy. The solid and short dashed line is the cross section calculated using the homogeneous function and using the inhomogeneous functions as given in Eq. (9). It is evident from this figure that the two methods are in very good agreement with each other. The long dashed curve is proportional to the amplitude for finding a photon at a frequency to excite the atom to the energies shown on the graph. This function was chosen to be proportional to $\exp[-(E-E_0)^4/\Gamma^4]$, where $E_0=-1.075 \times 10^{-3}$ a.u. and $\Gamma=1.2 \times 10^{-5}$ a.u.

There are basically only four states that are excited by the laser pulse. These states can be classified in terms of parabolic quantum numbers using the semiclassical wave func-

TABLE II. Classification of autoionizing states in Fig. 1.

n_ξ	n_η	n	E (10^{-3} a.u.)
16	2	20	-1.098
6	15	23	-1.091
12	7	21	-1.084
9	11	22	-1.078
17	1	20	-1.072
7	14	23	-1.066
13	6	21	-1.058
10	10	22	-1.050

tions. Before giving the classifications, we must stress that some of these states are strongly mixed and only the dominant contribution is given.

The classification of all of the states in Fig. 1 is given in Table II. Remember that n_ξ counts the number of nodes in the ξ direction, and n_η counts the number of nodes in the η direction and $n=n_\xi+n_\eta+|m|+1$. When $n_\xi \approx n$, the electron is localized on the up-field side of the atom. When $n_\xi \approx n_\eta$, the electron's motion is more nearly perpendicular to the field direction; i.e., the electron is localized to $z \approx 0$. Note that these states belong to different n manifolds. The main two states that are excited are the 12,7 and 17,1 states. We should expect that the main periodicity in the time-dependent flux should be $\sim 2\pi/\Delta E$, where ΔE is the energy difference of these two states. This ΔE is much smaller than the ΔE that arises from states of the same n . Therefore, we should see peaks in the flux with a larger spacing in time than would be expected from simple arguments based on energy splittings within an n manifold. Inspection of Fig. 1 leads us to expect that a laser pulse as sketched in Fig. 1 will produce a wave packet that has a periodicity in time given by $2\pi/\Delta E=5.2 \times 10^5$ a.u. = 12.7 ps. We expect the time-dependent flux to consist of relatively few pulses because the autoionizing states are very broad, and hence decay quickly.

However, there is some information that cannot be deduced. The most striking example is the relative heights of the electron pulses entering the detector. Will the electron pulse heights decrease monotonically with time, or will a more complex time dependence emerge? In Ref. [13], the recurrence spectrum for this system was measured. The recurrence spectrum measures $|\langle \psi(0) | \psi(t) \rangle|$, and may be obtained from the Fourier transform of the frequency-dependent photoionization cross section. Because the electrons can only scatter down-field and travel to the detector if they return to the nucleus, the plausible expectation is that detecting the time-dependent electron flux with an electron streak camera will simply reproduce the recurrence spectrum which can be obtained quite simply from Fig. 1. Lankhuijzen and Noordam [13] showed this expectation is wrong, and that interesting information is obtained with the streak camera that cannot be obtained in the energy domain.

In Fig. 2, we present the time-dependent flux as measured in Ref. [13] (solid line) and calculated using the homogeneous function from Eq. (7). This figure shows some of the expected features that can be obtained in the energy domain. The number and spacing of the peaks is as expected. Figure 2 also shows an interesting and unexpected feature. The heights of the peaks are very irregular with the second peak

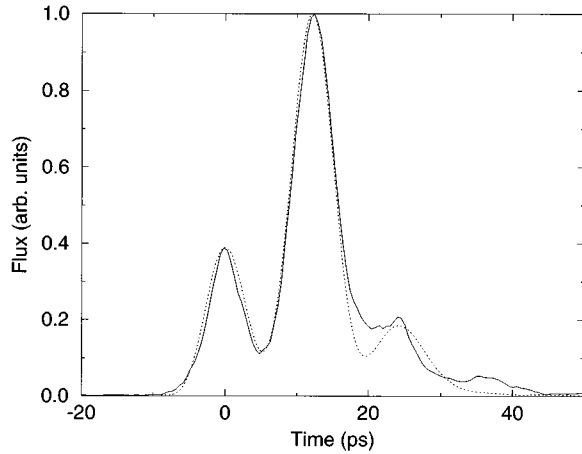


FIG. 2. The relative time-dependent flux using the pulse and field from Fig. 1. Solid line, experiment; dashed line, calculation using the homogeneous function. The time axes for all curves have been shifted so the first peak is at $t=0$.

being much higher than the first; in the recurrence spectrum, the first peak is the largest. The first peak results from the electrons that are excited directly down-field. The second peak results from electrons that are initially excited into a region of phase space that gives bounded motion. But after ~ 12 ps, the electron returns to the nucleus where it can be scattered into a different parabolic channel and travel to the detector. The third peak arises from electrons that were not scattered down-field during the first scattering with the core.

We have not included the calculation in Fig. 2 using the inhomogeneous function from Eq. (4). The two calculated fluxes are very close to each other; the slight differences could be explained as arising from slight inaccuracies in the different numerical methods. This means the electron waves disperse very little in traveling from ~ 2000 a.u. from the core into the detector which is a macroscopic distance from the atom. The time dependence of the electron flux entering the detector is an extremely accurate measure of the time dependence of the electrons being ejected from the atom. This fact is vitally important for the interpretation of the measurements. The reason for this lack of dispersion is that the electron is quickly accelerated in the electric field; the spread in the wave packet goes like $\Delta z = |t\Delta E/v|$, which goes to a constant at large t since $|v|$ is increasing linearly with t in the electric field.

The comparison of our calculations with experiment provides us with some information about the dynamics. We have gained information about the quality of WKB approximations, about the dispersion of the electron wave, and about the lack of importance of the spin-orbit interaction (we do not include the spin-orbit interaction in our calculation). There is further information that may be obtained because we can calculate the full wave function.

One aspect of our understanding may be tested using the WKB wave functions. This involves the expectation that the electron only escapes after it scatters from the core electrons. Equations (17) and (20) together give the transformation from the $\Psi_{E/m}$ functions to the $\Psi_{E\beta m}^-$ functions. We can reverse the transformation to calculate the relative probability for finding the electron in a particular ℓ wave within a

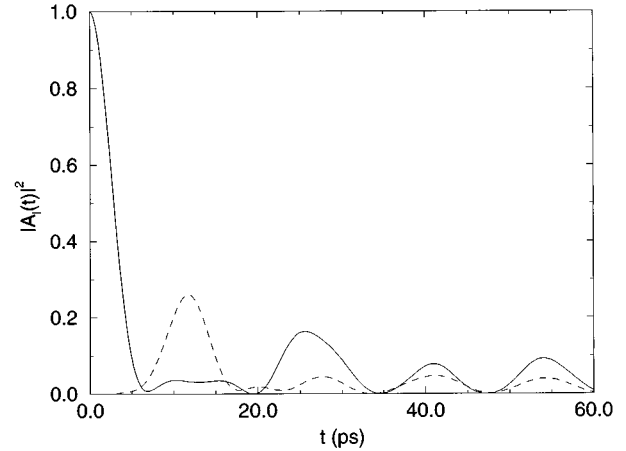


FIG. 3. The relative probability for finding the electron near the nucleus in a p wave (solid line) or a d wave (dashed line).

relatively small distance (e.g., 50 a.u.) from the nucleus. In Fig. 3, we plot the p -wave (solid line) and d -wave (dashed line) relative probabilities, written as $|A_\ell(t)|^2$, as a function of time. The p and d waves are the only $m=1$ waves that have quantum defects substantially different from 0. For the electron to scatter down-field, it must return to the core as a p - or d -wave. At $t=0$, there is a large p -wave component reflecting the initial excitation. At $t \approx 6$ ps and ≈ 20 ps, the p - and d -wave probabilities have become very small, and for $t \approx 13$ ps and ≈ 26 ps the p - and d -wave probabilities become large. It is an interesting feature that the first return ≈ 13 ps is dominated by d waves, and the second return ≈ 25 ps is dominated by p waves. This matches Fig. 2 in every respect.

However, there is not complete agreement between the two figures because near $t \approx 41$ ps and ≈ 54 ps, there are large recurrences of p - and d -wave characters. Actually these recurrences extend to very long times (67 ps, 80 ps, 92 ps, etc.). This behavior must come from the beating of the 9,11 and 7,14 states; these are very sharp, and thus have a long lifetime. This does not invalidate our argument about the mechanism for electrons leaving the atom. Electrons must return to the core in low- ℓ waves in order to scatter from one parabolic channel to another. In particular, the electrons must return to the core in order to scatter in to classically open channels and travel to the detector. But just because the electron wave returns to the core does not mean it will scatter *down field*. In Fig. 3, the relative proportion of p and d waves returning to the core is similar at 41 and 54 ps. The p and d waves do individually scatter from the core down-field. But the p and d waves are coherent, and the superposition of the p wave scattered down-field and the d wave scattered down-field destructively interfere giving only little flux into the detector. If we could change the phase of the p or d wave between 41 and 54 ps, we would obtain a large flux of electrons into the detector.

In Figs. 4, we present the contour plot of $\rho|\psi(\rho, z, t)|^2$ for several different times. The amount of wave function on the atom decreases with time so the peaks are rescaled at each t . There are a number of striking features of this figure. For example, we can clearly see the times when there is a large amount of flux of electrons leaving the atom. These figures

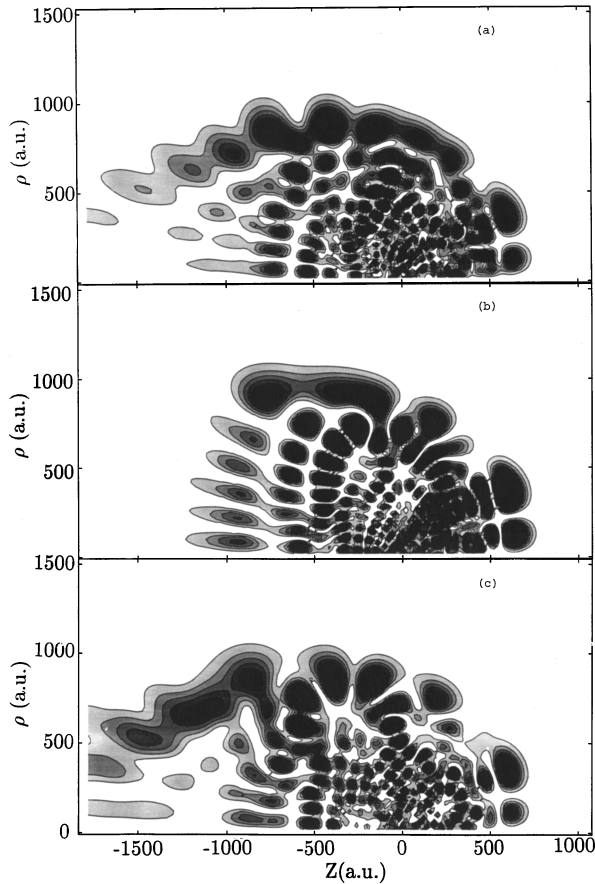


FIG. 4. Contour plot of $\rho|\psi(\rho, z, t)|^2$ at times (a) 0 ps, (b) 6 ps, and (c) 13 ps.

show quite a complicated spatial dependence of the wave packet. As an aid in the interpretation of this packet, we performed calculations of classical trajectories at this energy and field strength that start at the nucleus. In Fig. 5, we present five closed-orbit trajectories and the sequence of trajectories that directly escape the atom. A comparison of the general features between Figs. 4 and 5 sheds some light on the quantum processes.

As in Ref. [33], the flux going down-field does not cover all of the classically allowed region but is curiously confined. This confinement arises from the fact that the electrons traveling down-field must have originated from a scattering event near the nucleus. The quantum flux only covers the region of space which a classical electron could access if it started near the core. This effect is clear in Fig. 5(c), where the vast majority of the classical trajectories reach a maximum in ρ of 1000 a.u. near $z = -750$ a.u., and then decrease in ρ as z decreases. Compare this with Fig. 4(c) to see the similarity.

Some of the other features of the wave packet may be related to features of the closed-orbit trajectories. At $t = 6$ ps, there is a large amount of wave function down-field that is not traveling to the detector. The nodal structure indicates the main momentum component is in the ρ direction. In Fig. 5, we present some of the closed orbits at this energy. Notice that the simplest closed orbit [the bold line in Fig. 5(c)] spends most of its time at negative z , and goes through the antinodal structure of the wave functions.

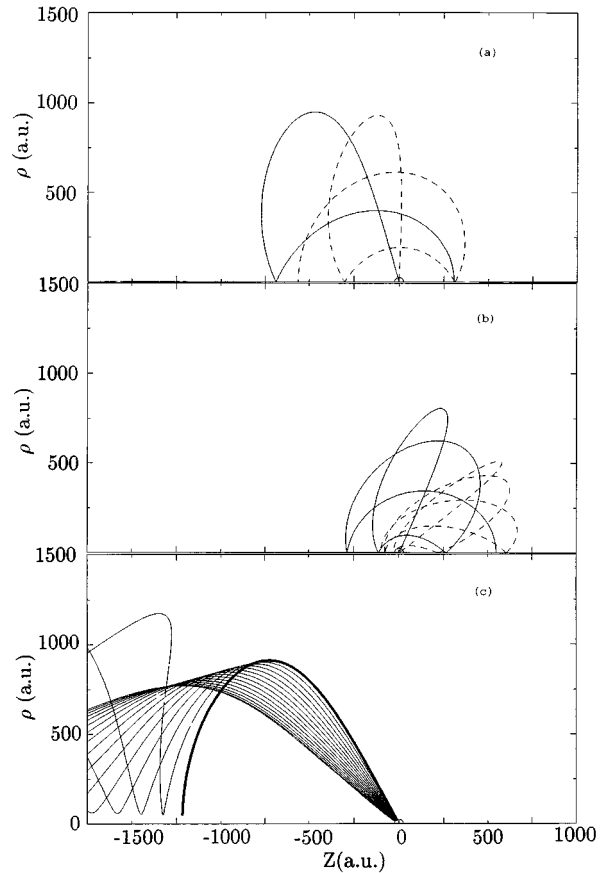


FIG. 5. (a) Two closed-orbit, classical trajectories that return to the nucleus after ≈ 6 ps. (b) Two closed-orbit, classical trajectories that return to the nucleus after ≈ 6 ps. (c) Bold line is a classical trajectory that returns to the nucleus after ≈ 6 ps. The thin line trajectories are those that leave the nucleus and travel down-field into the detector.

The connection between classical orbits and the quantum wave packets is somewhat more tenuous than the case discussed in Ref. [33]. There it was clear that only one orbit was important. Here all of the orbits that seem important have return times roughly a factor of 2 smaller than the quantum period. An interpretation of this system might invoke interference. We use Eq. (27) to calculate the semiclassical interference between returning orbits. Specifically, the two orbits in Fig. 5(a) have roughly the same return time, ≈ 6 ps, but return to the core out of phase with each other by 0.82π giving destructive interference. The two orbits in Fig. 5(b) have roughly the same return time, ≈ 6 ps, but return to the core out of phase with each other by 0.84π . Upon their second return to the core the orbits are now out of phase by $\approx 2\pi$, giving constructive interference. In the classical calculation, there are no closed orbits until the clustering of five orbits near 6 ps that are shown in Fig. 5; then there are no closed orbits until a clustering of nine orbits near 12 ps. These nine orbits are the second return of the five orbits in Fig. 5 and four new orbits returning for the first time.

This suggests that the period for this system is really near 6 ps, but an interference effect suppresses the wave packet near the core at the first return, and thus suppresses the scattering. An examination of the quantum energy levels in Table II supports this conjecture. If we use energy differ-

ences of autoionizing states of the same n , we find a period of roughly 6 ps. If we make one packet only out of $n=20$ states and a second packet only out of $n=21$ states, we would find that each of the packets would return to the nucleus after roughly 6 ps. However, because the $n=21$ states are nearly halfway between the $n=20$ states, we would find that there has accumulated roughly a π shift in phase between the packets, so that they destructively interfere near the nucleus. On their second return the relative phase would be roughly 2π , giving constructive interference.

VII. CONCLUSIONS

We have presented a theoretical exploration of the wave-packet dynamics for an electron excited from the ground state of Rb in a static electric field. We have compared the results of our calculations to the measured time-dependent flux of electrons into a detector a macroscopic distance from the atom. The good agreement indicates that the calculations have converged and are accurate, which indicates we can trust the dynamics that emerges from our calculated wave packets. The measurement of the ejected flux provides a new window for the observation of wave-packet phenomena. We have shown by direct calculation that the time-dependent flux measured at the detector accurately reproduces the flux that is leaving a sphere of 2000 a.u. centered at the nucleus.

This validates the promise of this type of measurement as a tool for investigating wave packets.

This system is interesting because it involves the wave-packet dynamics with two coupled spatial degrees of freedom. We have shown that it is possible to gain a detailed understanding of such systems by performing parallel quantum and classical calculations to uncover the mechanisms that guide the dynamics. There are several interesting features that emerge from the calculations for the particular case explored in Ref. [13]. The flux of electrons that leave the atom does not cover the full classically allowed region of space; the electrons only cover that region of space that a classical electron could reach if it started at the nucleus. We have also found that the period observed was twice as long as the classical closed-orbit period due to destructive interference, which reduces the probability for finding an electron near the nucleus at odd multiples of the period.

ACKNOWLEDGMENTS

We thank G. M. Lankhuijzen and L. D. Noordam for providing us with their experimental data, and for many profitable discussions. We gratefully acknowledge D. Harmin's help and insight. F. R. was supported by the NSF and J. S. by the U.S. Department of Energy.

-
- [1] A. ten Wolde, L. D. Noordam, A. Lagendijk, and H. B. van Linden van den Heuvell, *Phys. Rev. A* **40**, 485 (1989).
 - [2] J. A. Yeazell and C. R. Stroud, *Phys. Rev. Lett.* **60**, 1494 (1988); J. A. Yeazell, M. Mallalieu, J. Parker, and C. R. Stroud, *Phys. Rev. A* **40**, 5040 (1989).
 - [3] A. ten Wolde, L. D. Noordam, H. G. Muller, A. Lagendijk, and H. B. van Linden van den Heuvell, *Phys. Rev. Lett.* **61**, 2099 (1988).
 - [4] J. A. Yeazell, M. Mallalieu, and C. R. Stroud, *Phys. Rev. Lett.* **64**, 2007 (1990); J. A. Yeazell and C. R. Stroud, *Phys. Rev. A* **43**, 5153 (1991).
 - [5] J. A. Yeazell and C. R. Stroud, *Phys. Rev. A* **35**, 2806 (1987); *Phys. Rev. Lett.* **60**, 1494 (1988).
 - [6] X. Wang and W. E. Cooke, *Phys. Rev. Lett.* **67**, 1496 (1991); *Phys. Rev. A* **46**, 4347 (1992).
 - [7] L. D. Noordam, D. I. Duncan, and T. F. Gallagher, *Phys. Rev. A* **45**, 4734 (1992).
 - [8] B. Broers, J. F. Christian, J. H. Hoogenraad, W. J. van der Zande, H. B. van Linden van den Heuvell, and L. D. Noordam, *Phys. Rev. Lett.* **71**, 344 (1993); B. Broers, J. F. Christian, and H. B. van Linden van den Heuvell, *Phys. Rev. A* **49**, 2498 (1994).
 - [9] H. H. Fielding, J. Wals, W. J. van der Zande, and H. B. van Linden van den Heuvell, *Phys. Rev. A* **51**, 611 (1995).
 - [10] R. R. Jones, C. S. Raman, D. W. Schumacher, and P. H. Bucksbaum, *Phys. Rev. Lett.* **71**, 2575 (1993).
 - [11] D. W. Schumacher, J. H. Hoogenraad, D. Pinkos, and P. H. Bucksbaum, *Phys. Rev. A* **52**, 4719 (1995).
 - [12] G. M. Lankhuijzen and L. D. Noordam, *Phys. Rev. A* **52**, 2016 (1995).
 - [13] G. M. Lankhuijzen and L. D. Noordam, *Phys. Rev. Lett.* **76**, 1784 (1996).
 - [14] R. R. Jones, *Phys. Rev. Lett.* **76**, 3927 (1996).
 - [15] C. O. Reinhold, J. Burgdörfer, M. T. Frey, and F. B. Dunning, *Phys. Rev. A* **54**, R33 (1996).
 - [16] I. Sh. Averbukh and N. F. Perel'man, *Zh. Éksp. Teor. Fiz.* **96**, 818 (1989) [*Sov. Phys. JETP* **69**, 464 (1990)].
 - [17] R. Bluhm, V. A. Kosteletzky, and B. Tudose, *Phys. Rev. A* **52**, 2234 (1995).
 - [18] O. Knospé and R. Schmidt, *Phys. Rev. A* **54**, 1154 (1996).
 - [19] P. A. Braun and V. I. Savichev, *J. Phys. B* **29**, L329 (1996).
 - [20] C. Leichtle, I. Sh. Averbukh, and W. P. Schleich, *Phys. Rev. Lett.* **77**, 3999 (1996).
 - [21] H. H. Fielding, *J. Phys. B* **27**, 5883 (1994).
 - [22] O. Zobay and G. Alber, *Phys. Rev. A* **52**, 541 (1995).
 - [23] M. W. Beims and G. Alber, *J. Phys. B* **29**, 4139 (1996).
 - [24] K. Dupret and D. Delande, *Phys. Rev. A* **53**, 1257 (1996).
 - [25] D. W. Schumacher, D. I. Duncan, R. R. Jones, and T. F. Gallagher, *J. Phys. B* **29**, L397 (1996).
 - [26] D. I. Duncan and R. R. Jones, *Phys. Rev. A* **53**, 4338 (1996).
 - [27] F. Robicheaux and W. T. Hill III, *Phys. Rev. A* **54**, 3276 (1996).
 - [28] J. Zakrzewski, D. Delande, and A. Buchleitner, *Phys. Rev. Lett.* **75**, 4015 (1995).
 - [29] M. Kalinski and J. H. Eberly, *Phys. Rev. A* **52**, 4285 (1995).
 - [30] I. Bialynicki-Birula and Z. Bialynicki-Birula, *Phys. Rev. Lett.* **77**, 4298 (1996).
 - [31] (a) D. A. Harmin, *Phys. Rev. A* **24**, 2491 (1981); (b) **26**, 2656 (1982).
 - [32] U. Fano, *Phys. Rev. A* **24**, 619 (1981).

- [33] F. Robicheaux and J. Shaw, Phys. Rev. Lett. **77**, 4154 (1996).
- [34] W. Johnson, D. Kohb, and K.-N. Huang, At. Data Nucl. Data Tables **28**, 333 (1983).
- [35] U. Fano and A. R. P. Rau, *Atomic Collisions and Spectra* (Academic, Orlando, 1986); M. J. Seaton, Rep. Prog. Phys. **46**, 167 (1983).
- [36] M. L. Du and J. B. Delos, Phys. Rev. A **38**, 1896 (1988); M. L. Du and J. B. Delos, *ibid.* **38**, 1913 (1988).
- [37] J. Gao and J. B. Delos, Phys. Rev. A **46**, 1449 (1992).
- [38] J. Gao and J. B. Delos, Phys. Rev. A **49**, 869 (1994).
- [39] J. B. Delos, Adv. Chem. Phys. **65**, 161 (1986).
- [40] V. P. Maslov and M. V. Fedoriuk, *Semi-Classical Approximation in Quantum Mechanics* (Reidel, Boston, 1981).
- [41] J.-M. Mao, J. Shaw, and J. B. Delos, J. Stat. Phys. **68**, 51 (1992).
- [42] P. Dando, T. Monteiro, D. Delande, and K. T. Taylor, Phys. Rev. A **54**, 127 (1996).